Cooling by Discrete and Porous Injection into a Turbulent, Supersonic Boundary Layer

K. J. CLARK,* C. T. NARDO,* AND N. A. JAFFE†
Acurex Corporation, Mountain View, Calif.
AND
M. A. COVINGTON‡
NASA Ames Research Center, Moffett Field, Calif.

An experimental program was carried out to determine the local and downstream cooling effectiveness associated with injection of water through slotted and porous surfaces into a turbulent, supersonic boundary-layer. The experiments were performed in the NASA Ames 1 in.×5 in. turbulent duct facility, which provides stagnation enthalpies and pressures in the range 1200–2000 Btu/lbm and 34–50 atm. Flat-plate models were located downstream of the duct throat, where the Mach number and cold-wall heat flux were nominally 3.6 and 100 Btu/ft² sec. Instrumentation included pyrometry, slot in-depth thermocouples, color and infra-red photography, and downstream Gardon gages. The key experimental result was that the effective surface roughness at the injection region gives rise to augmented heating both locally and downstream for injection flow rates of interest.

Nomenclature

A_I = total surface area of injection region
F = normalized injection flux, $\dot{m}/\rho_e U_e$
h_0 = test-stream stagnation enthalpy
h_r = test-stream recovery enthalpy
h_w = wall enthalpy
Δh_v = coolant heat of vaporization
K = discrete roughness height
K_s = equivalent sand-grain roughness height
L = land streamwise width
M = coolant margin factor
M_{DS} = coolant margin for downstream heat flux threshold
M_p = coolant margin for pyrometer threshold
$\mathcal{M}_e$ = boundary-layer edge Mach number
$\dot{m}$ = coolant flow rate
$\dot{m}_i$ = ideal coolant flow rate
$\dot{m}_i''$ = ideal coolant flux based on total surface area of injection region
P_b = base pressure
P_e = boundary-layer edge static pressure
P_0 = test-stream stagnation pressure
$\dot{q}''$ = net heat flux to solid land or downstream surface
$\dot{q}_b''$ = blocked heat flux for smooth porous wall and continuous injection
$\dot{q}_0''$ = smooth wall, no-injection heat flux
S = slot streamwise width
St = smooth wall Stanton number with local or upstream injection
St_0 = smooth wall, no-injection Stanton number
T = slot in-depth temperature
T_p = pyrometer temperature
T_v = coolant vaporization temperature
U_e = boundary-layer edge velocity
U_{DSL} = dividing streamline velocity
W = slot transverse width
γ = specific heat ratio
θ = boundary-layer momentum thickness
θ_s = dividing streamline angle
ρ_e = boundary-layer edge density

Presented as Paper 74-98 at the AIAA 12th Aerospace Sciences Meeting, Washington, D.C., January 30–February 1, 1974; submitted February 25, 1974; revision received July 2, 1974. This research was performed under Air Force Contract F04701-71-C-0087. The authors wish to acknowledge the assistance provided by Dr. L. J. Alpinieri of Aerotherm in the design of the experimental program.

Index category: Boundary Layers and Convective Heat Transfer—Turbulent.

* Staff Engineer, Aerotherm Division. Member AIAA.
† Manager, Active Cooling Programs, Aerotherm Division.
‡ Research Scientist, Member AIAA.

Introduction

ACTIVE cooling by gas or liquid injection is an effective means for protecting surfaces exposed to high-temperature environments. In past applications, active cooling has been used to cool surfaces on re-entry vehicle nosetips, rocket nozzle throats, and turbine blades. Generally, active cooling techniques fall into two categories: transpiration cooling and slot film cooling. Slot film cooling relies upon the formation of a film which extends some distance downstream of the transverse injection slot and protects the downstream surface by quenching the boundary layer (cold gas injection) and/or absorbing heat by undergoing a phase change (liquid injection). The cooling effectiveness of the film diminishes in the downstream direction. In contrast, the transpiration cooling technique utilizes a porous surface which permits coolant to be injected over the entire area to be cooled. Local protection is provided by blockage due to blowing and, in addition, heat absorption due to phase change if the coolant is a liquid.

Usually, transpiration cooling is selected when the heating environments are especially severe and relatively large areas are to be cooled. Recently, however, the discrete injection (DI) concept, in which the coolant is delivered to the surface through many individual small slots or ports separated by solid lands, has been implemented in cooling surfaces exposed to high heating rates. The DI surface is a hybrid which combines features of both transpiration and slot film cooling. The small size of the slots (typically 0.005 in. width) approaches the scale of individual pores in a porous surface and the percent open area is large (nominally 50%). Also, some cooling downstream of each slot is required to protect the land surface area associated with each slot. Relative to the porous surface, two advantages commonly associated with the DI surface are 1) the coolant to each slot can be individually metered and controlled, thereby permitting control of the coolant distribution over the entire surface, and 2) in-depth vaporization of the (liquid) coolant can be accommodated without excessive pressure drop, thus allowing operation at higher surface temperatures and lower coolant flow rates.

Only recently have fabrication techniques advanced to the point where application of the DI method is feasible. Because

the method is relatively new and untried, the associated physics is not well understood and the cooling effectiveness is not well known. In particular, when the heating environment is a turbulent boundary layer, the question of heating augmentation due to the effective roughness of the surface arises. Also, the efficiency of heat transfer from slot walls to coolant is not known. Finally, a comparison of the cooling effectiveness of porous and DI surfaces under identical environmental conditions has not been reported in the open literature. Obviously, experimental data is required before these questions can be adequately addressed.

This paper summarizes an experimental investigation which was carried out to determine the local and downstream cooling effectiveness associated with injection of water through slotted (DI) and porous surfaces into a turbulent, supersonic boundary layer. All aspects of the experimental program are discussed at length in Refs. 1 and 2.

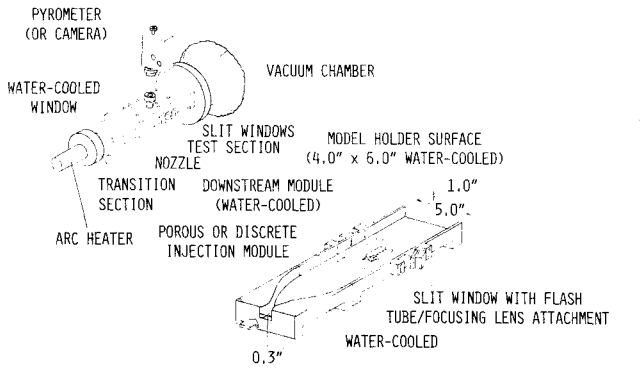

Fig. 1 Schematic of the arc-heated turbulent duct facility at NASA Ames Research Center, with Aerotherm model and instrumentation in position.

Experimental Apparatus

Scaling

In this study the heating environment of interest for application is a turbulent, supersonic boundary layer, providing a cold-wall heat flux of roughly 10^4 Btu/ft^2 sec. The pressure levels in the boundary-layer approach 100 atm, the surface material of interest is stainless steel, and the slot/land dimensions are nominally 0.005 in./0.010 in. This particular environment/surface combination is representative of a re-entry vehicle nosetip and associated aerodynamic heating. Precise duplication of the actual environment of interest in a ground test was anticipated to be both costly and difficult. Therefore, scaling techniques were utilized to permit conducting the experiment at lower heat flux and pressure levels.

Scaling of liquid layer, internal cooling, and external cooling phenomena were considered. The details of the scaling considerations are reported elsewhere (Refs. 1–3). Only a summary of the key results is presented here. It was concluded that simulation of liquid layer phenomena would be exceedingly difficult, because the present theories are inadequate for treating the occurrence of such phenomena under the conditions of interest. For instance, it is unlikely that a well-defined liquid film would even exist, because the minimum scale of surface roughness achievable with state-of-the-art fabrication techniques is greater than the extremely thin film thicknesses (of the order of 0.0001 in.) predicted by available theories. In view of these considerations, scaling of liquid layer phenomena was considered to be of secondary importance.

For scaling of internal heat transfer events below the exposed surface, the three important scaling parameters were found to be the net average heat flux reaching the exposed land surface area, the thermal conductivity of the land material, and the coolant flow rate. A simple coupled analysis of heat conduction in the solid land and convection between the coolant in a slot and the adjacent land was performed. It was found that both internal vaporization depth and land surface temperature were directly proportional to the three scaling parameters. The significance of this finding is that, from an internal cooling point of view, discrete injection phenomena at high heat flux conditions can be duplicated in a low heat flux experiment, provided that a land surface material with appropriately lower thermal conductivity is selected and lower coolant flow rates are utilized.

In considering the scaling of external cooling, two phenomena which influence the boundary layer formed over the exposed surface were investigated: heat flux blockage due to mass addition at the surface, and heat flux augmentation due to the effective surface roughness created by the presence of the slots. The smooth wall blockage correlation of Baronti et al.,[4] was used to demonstrate that the blocked value of heat transfer would not necessitate vanishingly small values of the coolant injection rate in order to attain high surface temperatures. For the low heat flux facility used in the experiment, the aforementioned correlation indicated the minimum value of $\dot{q}_b''/\dot{q}_0''$ would not be below 0.5.

Scaling of heating augmentation due to surface roughness involved consideration of the slot size relative to some parameter associated with the external boundary-layer thickness. Momentum thickness was chosen as the pertinent boundary length parameter, although the laminar sublayer thickness was also considered and resulted in conclusions which differed little from those based upon momentum thickness. Under the environmental conditions of interest, the ratio of boundary-layer momentum thickness to slot size is $0.1 < \theta/S < 1.0$ when $S = 0.005$ in. Thus, in order to properly scale the effective surface roughness under conditions of interest, the slots in the test model were selected based upon consideration of the momentum thickness of the test stream boundary layer and the above range of θ/S.

Test Facility

Based upon the findings of the scaling analysis, it was determined that the test facility must provide a turbulent, supersonic boundary layer with a cold-wall heat flux high enough to achieve elevated land surface temperatures and slot in-depth vaporization for low (but finite) coolant flow rates. The facility selected for the present experimental program was the NASA Ames 1 in. × 5 in. turbulent duct facility, a schematic of which is presented in Fig. 1. This facility has the desired characteristics and, moreover, it is the only arc-heated duct available which has been deomonstrated to have a turbulent boundary layer over the test section.[5]

A Linde N-4000 high-pressure arc heater is used to provide a high temperature air stream for the water-cooled duct. The internal configuration of the test section is rectangular with a 1 in. × 5 in. cross section. The test model is inserted into the floor of the duct, and 7 Gardon gages and 8 wall pressure taps are located in the ceiling of the duct. In the present study, the third Gardon gage downstream was removed and replaced with a water-cooled window assembly for overhead pyrometry and photography. Three slit windows are mounted on each side of the duct at the test section for test stream and model observation. One of the center windows was replaced with a special window with attached flash tube which provided illumination when color photographs of the injection module surface were taken. A Beckman ANSCAN Digital Recording System was used to record the heat flux and temperature data at each steady-state condition over a 10 sec interval at a sampling rate of 3 per sec.

Models

A sketch of the model assembly which was mounted in the floor of the duct is presented in Fig. 2. A copper, water-cooled model holder with 4 in. × 6 in. test surface interfaced with the opening in the floor of the duct. The actual model within the model holder was comprised of two major components: the

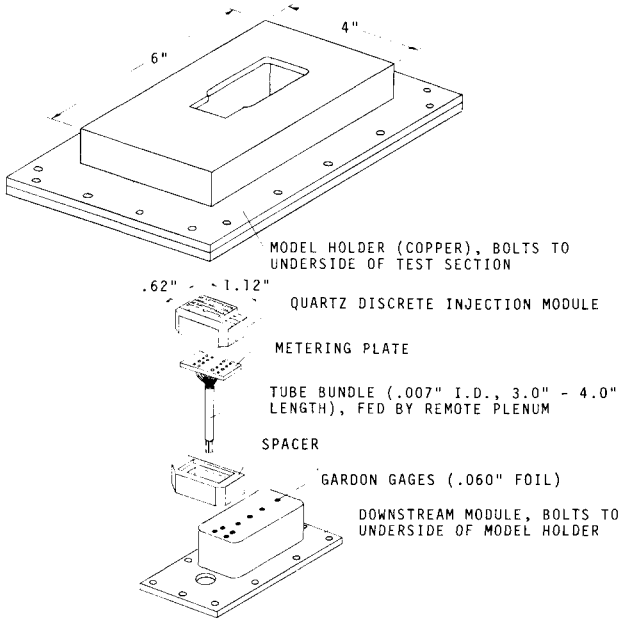

Fig. 2 Schematic of model assembly.

injection module (discrete or porous), and the downstream module.

The discrete injection module was fabricated from solid quartz stock. Quartz was chosen solely because its thermal conductivity of 0.8 Btu/ft-hr-°F is approximately 20 times lower than that of stainless steel, thereby permitting approximate scaling of internal cooling phenomena in the test facility where the heat flux is roughly two orders of magnitude below the heat fluxes of actual interest. The basic DI module fabrication procedure was to first grind channels in several identical quartz platelets, and then stack these platelets together to form a slotted block of quartz. When the quartz DI module was inserted in the model holder, each platelet was allowed to float free from adjacent platelets in order to reduce the possibility of thermal stresses developing, which would result in fractures. The external faces of the assembled module were coated with a thin layer of RTV adhesive/sealant.

Table 1 summarizes the matrix of slot/land dimensions considered in the experimental program. The slots were staggered from row to row. The smallest S/L combination duplicated the dimensions expected for use in the 10^4 Btu/ft^2 sec environment. The largest value of S was chosen to approximately scale the test value of θ/S within the range associated with the high-pressure, high-heat-flux environment ($0.1 \leqq \theta/S \leqq 1.0$). In the test duct, $\theta \simeq 0.1$ in. The outer dimensions of the injection area were identical for all injection modules: 1.12 in. in the transverse direction, and 0.62 in. in the streamwise direction. Because this

Table 1 Slot/land matrix

S (in.)	L (in.)	W (in.)	S/L (−)	Percent Open area (%)	Number slots/row (−)	Number rows (−)
0.010	0.020	0.100	0.5	33.3	10	20
0.051	0.051	0.485	1.0	50.0	2	6
0.051	0.102	0.485	0.5	33.3	2	4
0.102	0.051	0.485	2.0	66.7	2	4

area was always the same, the total mass flow rate (lbm sec) injection for a specified average coolant mass flux (lbm/ft^2 sec) was independent of the S/L configuration. This simplified the interpretation of data obtained on the downstream cooling effectiveness and eliminated the need for major coolant capacity variations for the different injection modules.

For the DI modules with $S \geqq 0.051$ in., metering plates were constructed from 0.007 in. ID hypodermic tubing. Two tubes fed each full slot and one tube fed each half slot. For the $S = 0.010$ in. module, a porous stainless steel plate was used to meter the coolant flow just upstream of the slots.

The porous models used in the transpiration cooling tests were fabricated from a rigidized fibrous material manufactured at NASA Ames. This low density (28 lbm/ft^3) material consists of short, 1 μ diam, high-purity silica fibers bonded together with colloidal silica to form a rigid 100% open cell matrix having low thermal conductivity.

The downstream module was fabricated from copper and had its own coolant circuit. In addition, it was instrumented with 8 Gardon gages positioned as indicated in Fig. 2. These gages are discussed in greater detail later.

A variable-back-pressure coolant supply system was used for the injection module. Variations in the coolant flow rate were accomplished by varying the reservoir pressure, which eliminated the long transients typical of a low-flow-friction system. In addition, a large-pressure-drop valve was located immediately upstream of the injection module to maintain a major portion of the coolant supply system above atmospheric pressure and thereby prevent the formation of large air voids in the lines.

Instrumentation

Pyrometer

The average surface temperature at the center of the injection module was measured with a Thermodot Model TD-17G pyrometer positioned as indicated in Fig. 1. Since the spot size for the pyrometer was 0.1 in. × 0.1 in., several lands were in the field of view on the $S = 0.010$ in./$L = 0.020$ in. DI module, and a single land was viewed on the remaining modules. The spectral range of the pyrometer was 3.5 to 4.1 μ, and the temperature range was 850 to 5171°R. The pyrometer was calibrated in bench tests which utilized a full-sized plywood model of the turbulent duct test section and a thermocouple-instrumented quartz module which was heated with a welding torch. The calibration data indicated that the spectral emissivity of the quartz surface was essentially unity. However, the effective aperture of the pyrometer was limited by the 0.2 in. I.D. water-cooled sapphire window, with the result that the effective surface emissivity was reduced to 0.385.

Slot in-depth thermocouples

Temperatures and temperature gradients in selected coolant channels of the DI modules were monitored with thermocouples. Each instrumented slot had three iron/nickel junctions, at three different depths below the surface ranging from 0.008 to 0.060 in. The bimetal junctions were vacuum-deposited onto the upstream side of selected lands. A protective coating of silicon monoxide was deposited over the metal thin films. Varnished lead wires with a 0.002 in. diam were soldered to the thin films at the upstream side of the slot, where temperatures were always low due to the presence of the liquid phase coolant and the fact that heating from the test stream could not penetrate to the bottom of the slots.

Color photography

During selected test runs, the state of the coolant at the surface in the center of the injection module was monitored with color sequence photography. A remote-controlled Nikon F 35 mm camera was used. A 135 mm lens with a 16 in. extension provided roughly 3× magnification with a depth of field of approximately ±0.020 in. The synchronized electronic flash unit mounted to the slit window in the side of the duct (see Fig. 1) provided an exposure time of 1/1000 sec. Kodak High Speed

Table 2 Test matrix

Run No.	Model configuration	Window diagnostic	h_o (Btu/lbm)	P_o (atm)	M_e (−)	$\dot{q}_o''$ (Btu/ft² sec)	$\dot{m}_i$ (lbm/sec)
1	$S = 0.010$ in./$L = 0.020$ in.	Pyrometer	2050	34.0	3.52	102.0	2.57×10^{-4}
2	↓	Infrared	2100	34.0	3.58	108.0	2.72
3	↓	Infrared	2150	33.8	3.64	132.0	3.30
4	↓	Color	2150	34.0	3.65	126.0	3.15
5	$S = 0.051$ in./$L = 0.051$ in.	Pyrometer	2150	34.0	3.65	115.0	2.89
6	↓	Pyrometer	1885	34.0	3.47	90.5	2.40
7	↓	Infrared	1950	34.4	3.47	87.4	2.23
8	↓	Color	1950	34.0	3.47	87.4	2.23
9	$S = 0.051$ in./$L = 0.102$ in.	Pyrometer	2050	34.4	3.48	97.7	2.47
10	↓	Infrared	2100	33.7	3.47	97.7	2.47
11	↓	Color	2150	33.8	3.47	99.4	2.49
12	$S = 0.102$ in./$L = 0.051$ in.	Pyrometer	1850	47.6	3.60	95.6	2.54
13	↓	Infrared	1825	46.9	3.51	95.6	2.54
14	↓	Color	1900	47.6	3.50	107.0	2.77
15	$S = 0.010$ in./$L = 0.020$ in.	Pyrometer	1900	47.6	3.58	95.8	2.49
16	↓	Infrared	1725	46.9	3.56	101.0	2.72
17	↓	Color	1800	47.3	3.56	101.0	2.72
18	↓	Color	1675	47.6	3.58	101.0	2.87
19	↓	Infrared	1650	47.5	3.58	96.8	2.75
20	Uncooled Teflon	Color		Transient			
21	Uncooled Teflon	Infrared		Transient			
22	Porous	Pyrometer	1700	47.6	3.53	95.8	2.71
23	↓	Pyrometer	1800	46.6	3.59	94.5	2.55
24	↓	Infrared	1100	46.9	3.41	68.5	2.18
25	↓	Color	1200	46.9	3.59	67.6	2.09

Ektachrome (ASA 160) color slide film with standard Kodak processing was used.

Infrared photography

Infrared photography was used to provide a quantitative estimate of the temperature variations over the surface of the injection module. The camera arrangement described in the previous paragraph was also used for the infrared photography, without the flash tube and with the addition of a Nikon R60 (red) filter. Kodak High Speed Infrared film (black and white) was used in conjunction with an f5.6 aperture and three shutter speeds of 1, 3, and 10 sec. The lower end of the spectral range was approximately 0.62 μ, all shorter wavelengths being eliminated by the red filter. The upper limit of the spectral range was approximately 0.95 μ, since the film sensitivity drops off rapidly for longer wavelengths. Absorption and emission in this spectral regime by the test stream and injected water (liquid and/or vapor) was estimated to be negligible. In addition, for this spectral regime and the temperature range of interest ($400 \leqq T \leqq 1500$°F), it can be shown that the inverse of the surface temperature is a linear function of the exposed film density, providing that the surface emissivity is a constant. The pyrometer measurements were used to provide a calibration between film density and surface temperature. An International Imaging Systems microdensitometer was used for all film density measurements.

Flow metering

Total flow rate to the injection module was monitored with bench-calibrated rotameters. Two SK type 20-7050 V rotameters were used, with ranges of 0.0 to 60 cc/min (0.0 to 2.2×10^{-4} lbm/sec) and 0.0 to 60.0 cc/min.

Metering plates were installed upstream of the slotted DI modules. The pressure drop across the metering plate was deliberately high, so that the coolant flow rate to each slot would be unaffected by the occurrence of any phenomena which would serve to change the slot pressure drop, such as boiling in the slots or pressure nonuniformities in the free stream. The hypodermic tube lengths used in the metering plates were individually calibrated. The tube-to-tube variation in flow rate vs pressure drop did not exceed 15%. The porous steel metering plate used for the module with $S = 0.010$ in. was found to have flow nonuniformities; however, they did not exceed $\pm 30\%$, and the local variations over the metering plate were well characterized in bench tests.

At the maximum coolant flow rate considered, the pressure drop across the porous module was approximately 4.0 psi. This pressure drop was sufficiently high that no additional metering was required. Physical permeability of the porous module was determined in bench tests to be in the range $1.42\text{–}1.53 \times 10^{-11}$ ft².

Downstream Gardon gages

The downstream module was instrumented with Gardon gages having a 0.125 in. body diameter and a 0.060 in. foil diameter. A total of eight gages was used, with the first four staggered to achieve a maximum packing density at the leading edge of the module. The downstream module and associated gages were fabricated and calibrated by Thermogage, Inc.

Miscellaneous instrumentation

Cold wall, no-injection heat flux and wall static pressure were measured with the Gardon gages and pressure taps mounted in the wall opposite the model assembly. Arc heater chamber pressure, power input, and test gas mass flow rate were measured in order to permit calculation of the total mixed-mean enthalpy and static and total properties at the test section.

Experimental Data

A total of twenty-five test runs was performed. During a given test, either pyrometry, color photography, or infrared photography was used in conjunction with the water-cooled window on the top wall of the duct. The availability of only one such window prevented simultaneous utilization of all three diagnostics. Each test run started at the high end of the coolant flow rate range where surface temperatures at the injection module were below the coolant vaporization temperature. Data were then collected at a series of 4–8 flow rates in descending order. Approximately 1 min was allowed after each flow rate adjustment in order to achieve steady-state conditions.

In addition to the DI and porous models, two Teflon models were tested. These models had a 4.0 in. × 6.0 in. surface area and replaced the entire model assembly in the duct wall. The purpose in testing the Teflon models was to investigate the extent and degree of test stream heat flux nonuniformities over

the test section, by observing the ablation patterns after a 30 sec exposure. No unacceptable variations in the heat flux were indicated from these tests.

Table 2 summarizes the test matrix. Stagnation enthalpy h_0 was determined as a function of duct throat area, total mass flow rate, and chamber pressure from the sonic flow method.[6] Mach number M_e and other total and static properties of the test section were determined from the equilibrium air tables of Refs. 6 and 7, the experimental pressure ratio P_w/P_0, and the sonic-flow-calculated value of h_o. The ideal coolant flow rate $\dot{m}_i$ is defined as the coolant flow rate necessary to precisely offset the blocked heat flux by vaporization of the coolant, assuming continuous injection from a smooth porous surface. Thus,

$$\dot{m}_i = \dot{m}_i'' A_I \tag{1}$$

where

$$\dot{m}_i'' = \dot{q}_b''/\Delta h_v \tag{2}$$

and A_I is the total area of the injection region, nominally 0.62 in. × 1.12 in. The ratio $\dot{q}_b''/\dot{q}_o''$ was taken to be equal to St/St_o, where the latter quantity was obtained from the aforementioned smooth wall blockage correlation for water vapor injection into a turbulent, supersonic air boundary layer.[4] The nondimensional injection rate used in conjunction with the blockage correlation was determined from

$$F/St = \frac{\dot{m}_i''}{\rho_e U_e St} = \frac{\dot{m}_i''(h_r - h_w)}{\dot{q}_b''} = \frac{h_r - h_w}{\Delta h_v} \tag{3}$$

where Reynolds' analogy is assumed, and $\Delta h_v \simeq 1000$ Btu/lbm and $h_w \simeq 150$ Btu/lbm at the water saturation temperature corresponding to the average measured wall static pressure (0.30 atm).

Figure 3 summarizes the pyrometer data taken during the experimental program. The margin factor M is defined as

$$M \equiv \dot{m}/\dot{m}_i \tag{4}$$

where $\dot{m}$ is the experimentally measured flow rate. Due to the definition of $\dot{m}_i$, the margin factor implicity accounts for variations in test conditions ($\dot{q}_o''$) from run to run. Also, choosing to define M in this manner delineates the effects of surface roughness, which is the principal difference between DI and porous surfaces as far as the external boundary layer is concerned. The most distinctive feature of Fig. 3 is that the porous module was much more thermally efficient than any of the slotted modules, because surface temperature lift-off occurred at significantly lower margins. In fact, the porous module performed very close to theory, since an extrapolation of the $T_p(M)$ curve to $T_p \simeq 150$°F (the water saturation temperature at test conditions) gives a margin factor very close to unity. The poorer performance of the slotted modules is attributed to augmented heating developed at the injection surface due to its roughness. In addition, the temperature lift-off appears to be a function of the relative roughness of the DI surface, as discussed later. One other significant feature of Fig. 3 is that the slope dT_p/dM is noticeably steeper for the porous module.

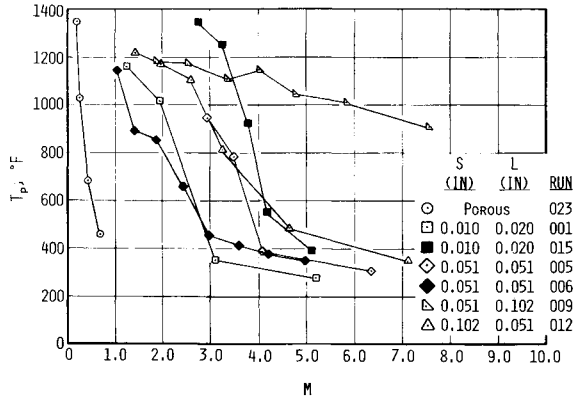

Fig. 3 Surface temperature vs margin factor.

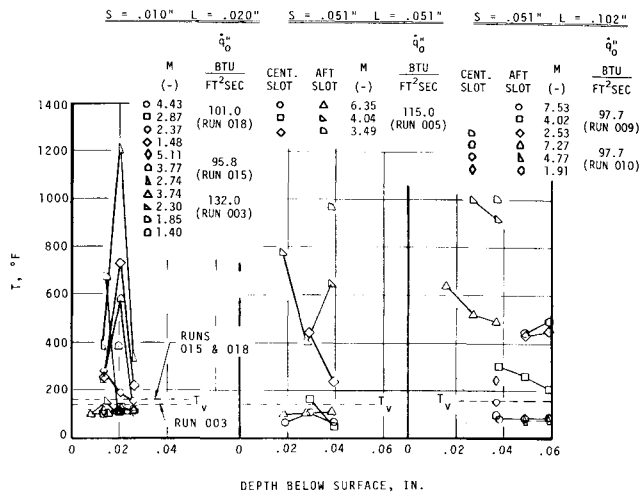

Fig. 4 Slot in-depth temperatures vs depth below surface and margin factor.

Figure 4 summarizes the slot in-depth data. The primary significance of this data is that once the coolant margin drops below 2.0 for the $S = 0.010$ in./$L = 0.020$ in. module and below 4.0 for the modules with larger slots, the in-depth temperatures (from 0.003 in. to 0.060 in. below the surface) are greater than

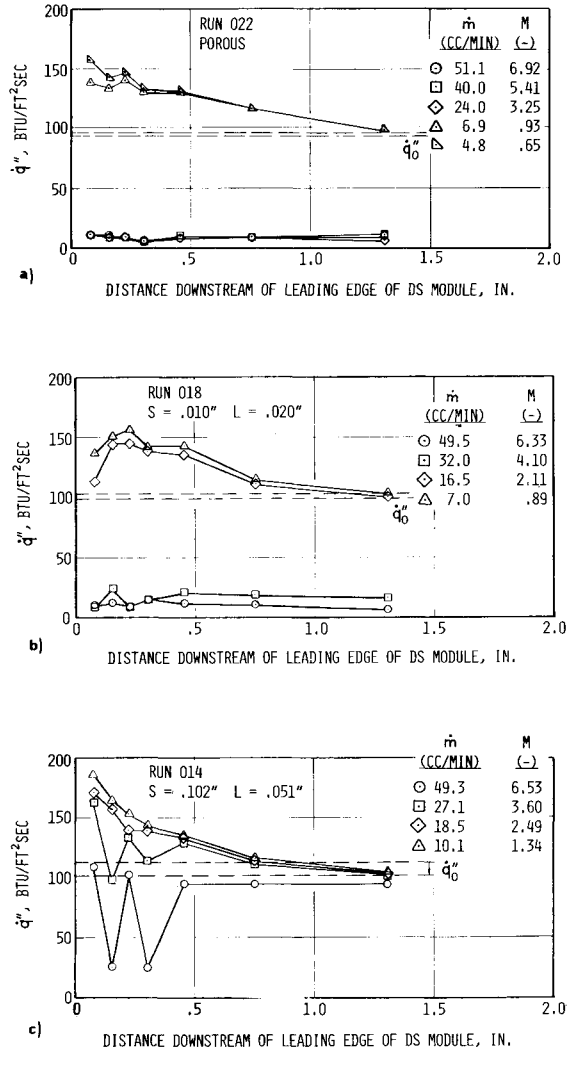

Fig. 5 Downstream heat flux distribution vs margin factor.

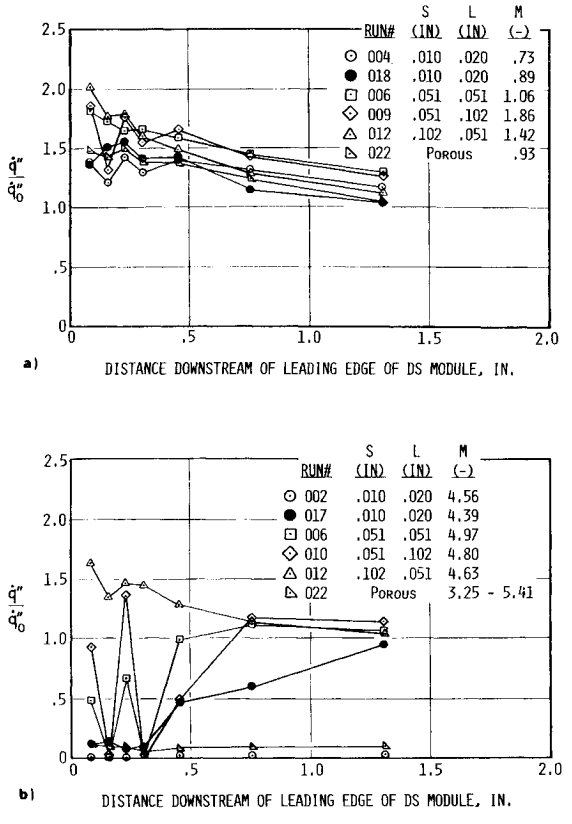

Fig. 6 Normalized downstream heat flux distributions a) at $M \simeq 1.0$ and b) at $M \simeq 4.5$.

the coolant vaporization temperature. If the surface roughness were not a factor, these temperatures would have remained at or below T_v for $M \geqq 1.0$.

The in-depth and surface temperature data of Figs. 3 and 4 indicate the occurrence of random hot spots. For instance, during Run 15 the surface and intermediate-depth slot temperature reached much higher temperature levels at a given flow rate than in Runs 1 and 3 involving the same S and L dimensions and heat flux levels. The intermediate-depth thermocouple junction was located on the opposite side of the slot from the other two junctions. Apparently, then, coolant nonuniformities within a single slot were large enough to result in a portion of the slot being relatively uncooled. The hot spot phenomena also occurred for the $S = 0.051$ in./$L = 0.102$ in. module during Runs 9 and 10. In these runs (as in all runs), the pyrometer was aligned over the center slot, rather than the aft slot. During Run 9, both surface and in-depth themocouples indicated unusually high temperatures even at the highest flow rate. However, in the following Run 10 the surviving slot thermocouples indicated much lower temperatures for the same coolant flow rate range.

Figure 5 presents a portion of the downstream heat flux data obtained from the experimental program. For the porous and $S = 0.010$ in./$L = 0.020$ in. modules, good downstream cooling for two to three injection lengths was achieved for $M \geqq 3.0$, while the module with $S = 0.100$ in. did not provide effective downstream cooling even for $M = 6.5$. As was the case with the pyrometer data, these results appear to be a function of effective roughness at the injection section. Also, it is noted that the peak heating near the leading edge of the downstream module at low values of M appears to increase with increasing injection surface roughness. The sawtooth appearance of the downstream heat flux distribution at intermediate coolant flow rates is most likely a result of the staggered position of the first four Gardon gages and the presence of a slight swirl or tangential velocity component in the test stream.

Figure 6 is presented to permit comparison of downstream cooling performance from module to module and further delineates roughness effects. At $M \simeq 4.5$, the modules with the lowest effective surface roughness provide good downstream cooling, while the rougher modules give downstream heating enhancement up to 1.6 times the cold-wall value. At $M \simeq 1.0$, none of the modules provides downstream cooling, and the peak heating increases as the effective surface roughness increases. Note that even for the smooth porous module downstream heating is significantly higher than the cold wall value when M is low. This is because the downstream module is water cooled so that its surface is relatively cold, while the surface at the injection region is hot if M is low. It can be shown theoretically that a hot upstream running length results in enhanced heating from the boundary layer when it reaches the cooled surface.

Numerous color and infrared photographs were obtained during the testing. Samples of these photographs are available in Refs. 1 and 2; the results are only summarized here due to space limitations. The color photographs revealed the appearance of the injection surface and the coolant in the vicinity of the slots under various flow rate conditions. The photographs indicate that under no conditions, including injection into a cold test stream from the smooth porous module, is a smooth liquid layer formed. At high margins with a hot test stream, the coolant was entrained into the boundary layer in the form of a mist or tiny liquid-phase droplets. Also, at high margins and with $S \geqq 0.051$ in. the liquid-phase coolant below the slot exit plane did not entirely fill the slot. Rather, "threads" of liquid coolant usually attached themselves to the webs separating adjacent slots located at the same streamwise station. As the margin decreased to 3.5–4.0, evidence of mist entrained into the boundary layer diminished, implying that all coolant entering the boundary layer was then in the vapor phase. At $M = 1.0$–1.5, there was no evidence of liquid-phase coolant above or even to some distance below the slot exits, and the red-hot appearance of the lands indicated they attained elevated temperatures (substantiated by the pyrometer data).

The infrared photographs revealed both global and local temperature variations. First, there were large-scale nonuniformities in the surface temperature at low coolant margins, for both DI and porous surfaces. For the DI modules, this was due to uneven coolant distribution within a single slot for the larger-slot modules, and uneven slot-to-slot metering for the $S = 0.010$ in. module. Variations in local permeability were most likely the cause of temperature variations over the surface of the porous module. Generally, the web separating two adjacent slots at the same streamwise position was the coolest region on the surface. This was most likely due to two effects: the coolant in the slots tended to adhere to the sides of the webs, and the web did not have an exposed leading edge which experienced enhanced heating similar to that which occurred on the lands.

On a smaller scale, the infrared photographs revealed that very small surface imperfections, much smaller than the land width, experienced enhanced heating. Also, on a single land peak temperature was slightly downstream of the leading edge, smaller lands exhibited steeper surface temperature gradients, and the decay in the downstream direction from the peak temperature was nearly linear for all land sizes.

Supporting Analysis

Since the results of the experimental investigation revealed that cooling performance is sensitive to injection surface roughness, an attempt was made to quantify the degree of surface roughness for correlation purposes. An extensive analysis of both roughness and roughness-augmented heating relative to this program has been performed and will appear in a later paper.[10] Only the surface roughness parameter is discussed here.

A technique was developed in which an equivalent sand-grain roughness value could be identified with a given discrete injection surface geometry. By assigning a roughness value to a

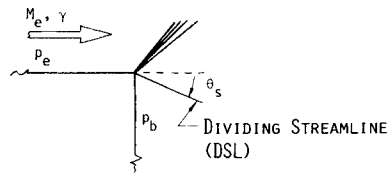

Fig. 7 Chapman-Korst inviscid base flow model.

given surface, over-all performance can be rated as a function of roughness severity. Since discrete injection surfaces are infinite in depth with respect to the length scale of the boundary-layer, it was first necessary to assign a physical roughness height to each slot opening. This was accomplished by considering the separation angle made by the dividing streamline as it leaves the sharp edged surface and enters a cavity or slot (Fig. 7). Knowing the edge pressure and edge Mach number, an expression for P_b as a function of P_e, $\mathcal{M}_e$, and U_{DSL}/U_e can be developed for $\dot{m} = 0$, namely[8]

$$\frac{P_b}{P_e} = \left\{\frac{1+[(\gamma-1)/2]\,\mathcal{M}e^2}{1+[(\gamma-1)/2][\mathcal{M}_e{}^2/(1-\phi^2)]}\right\}^{\gamma/\gamma-1} \tag{5}$$

where $\phi = U_{DSL}/U_e$.

The value of ϕ can be obtained from an analysis of the viscous shear layer which surrounds the dividing streamline. Such an analysis has been performed, and the resulting solutions for laminar and turbulent flow analyses are given in Ref. 8. Once the base pressure is determined, the flowfield can be expanded through a Prandtl-Meyer expansion fan corresponding to the base pressure expansion and, hence, θ_s can be calculated. Assuming that the dividing streamline is approximately linear (a fairly good assumption for small cavity spans and no injection), one can then calculate the discrete roughness height from

$$K = \tan\theta_s * S \tag{6}$$

where S is the slot opening. An equivalent sand-grain roughness height, K_s, can then be obtained from, for example, Ref. 9. The value of K_s is not solely a function of the slot opening but, in addition, must account for the wavelength effect of multiple slots. For example, for a given slot opening, one would expect the equivalent sand-grain roughness to be smaller for larger values of the wavelength, where the wavelength is defined as the summation of one pair of slot and land lengths.

Each of the discrete injection modules can be assigned an equivalent sand-grain roughness value. Figure 8 illustrates the usefulness of the roughness parameter K_s in correlating the pyrometer temperature liftoff for all injection modules tested. Liftoff was defined to occur when the measured surface temperature

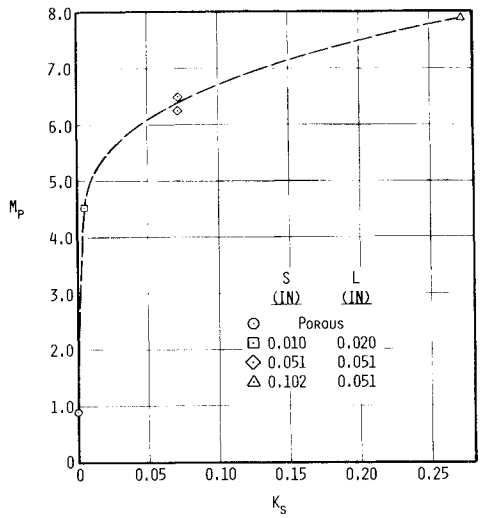

Fig. 8 Margin at T_p = 300°F vs equivalent sand grain roughness.

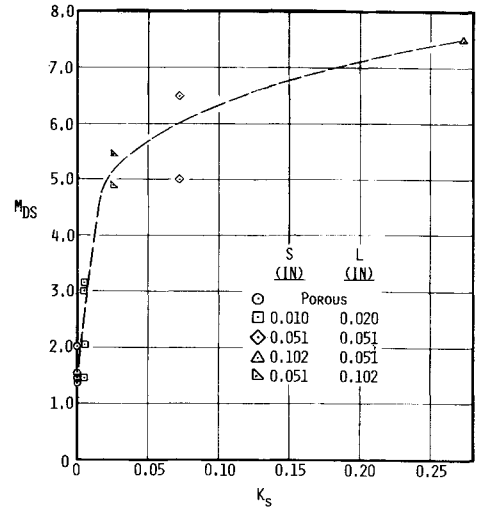

Fig. 9 Margin at downstream threshold vs equivalent sand grain roughness.

reached 300°F. The data of Runs 9 and 15 were excluded from this correlation, since they are associated with the hot-spot phenomena discussed above. The correlation reveals that with increasing surface roughness the coolant flow rate required to maintain the surface at 300° F first increases very rapidly and then approaches an asymptotic value of about 9.0.

Figure 9 is a similar threshold or liftoff margin correlation which utilizes the downstream heat flux data. The downstream threshold margin is defined as the approximate margin at which most of the Gardon gages change from indicating low heat fluxes (~10 Btu/ft^2 sec) to indicating high heat fluxes (~100 Btu/ft^2 sec). As demonstrated by the data presented in Fig. 5, this decrease in downstream cooling effectiveness occurs over a relatively narrow coolant flow rate range. Again, an asymptotic margin of about 9.0 is approached.

Summary and Conclusions

An experimental program has been carried out to investigate the local and downstream cooling effectiveness of the discrete injection cooling method. A porous model was also tested to provide a direct comparison of injection from slotted and smooth surfaces under identical test conditions. The environment of interest, a turbulent, supersonic boundary layer with a cold wall heat flux of approximately 10^4 Btu/ft^2 sec, provides heating levels typically experienced by a re-entry vehicle nose cone. However, a scaling analysis was performed to demonstrate that an economical, low-heat-flux test facility ($\dot{q}_o'' \simeq 100$ Btu/ft^2 sec) could be used to provide the proper simulation as long as models with low thermal conductivity were used. The selection of four slot/land combinations was based on a scaling analysis of relative surface roughness, which considered the ratio of boundary-layer momentum thickness to slot width.

Three primary conclusions have been derived from the experimental data and supporting analysis. 1) Roughness of the injection surface reduces both local and downstream cooling efficiency. 2) Hot spots can develop on both DI and porous surfaces due to coolant distribution nonuniformities. 3) Even at high coolant margin factors (~8.0), the formation of a cohesive liquid layer does not occur.

In the analysis portion of the investigation, an inviscid base flow model was used to determine the position of the dividing streamline over a slot. This, in turn, was used to determine the effective roughness height presented by the slot opening. The computed roughness height was then converted into an equivalent sand-grain roughness, and this latter parameter was found to correlate both pyrometer temperature liftoff and downstream heat flux liftoff.

References

[1] Jaffe, N. A., Clark, K. J., Nardo, C. T., and Anderson, L. W., "Nosetip Cooling Technology Program," Final Report 73-84, Air Force Contract F04701-71-C-0087, Oct. 1973, Aerotherm Div., Acurex Corp., Mountain View, Calif.

[2] Clark, K. J. and Mehner, P. O., "Test Report, Nosetip Cooling Technology Program, Combined Cooling Tests," Air Force Contract F04701-71-C-0087, Sept. 30, 1974.

[3] Lane, F., "Liquid-Layer Phenomenology," KLD TR-6, Feb. 1972, KLD Associates, Huntington, New York.

[4] Baronti, P., Fox, H., and Soll, D., "A Survey of the Compressible Turbulent Boundary Layer with Mass Transfer," *Astronautic Data*, Vol 13, 1967, pp. 239–249.

[5] Covington, M. A. and Vojvodich, N. S., "Turbulent Flow Studies in Two Arc-Heated Duct Facilities," *Journal of Spacecraft and Rockets*, Vol. 9, No. 6, June 1972, pp. 441–447.

[6] Jorgensen, L. H. and Baum, G. M., "Charts for Equilibrium Flow Properties of Air in Hypervelocity Nozzles," TND-1333, 1962, NASA.

[7] Moeckel, W. E. and Weston, K. C., "Composition and Thermodynamic Properties of Air in Chemical Equilibrium," TN-4265, 1958, NACA.

[8] Charwat, A. F., "Supersonic Flows with Imbedded Separated Regions," *Advances in Heat Transfer*, Vol. 6, Academic Press, New York, 1970, pp. 1–132.

[9] Schlichting, H., *Boundary Layer Theory*, 4th ed., McGraw-Hill, New York, 1960.

[10] Nardo, C. T., "Discrete Injection Blockage Condition," Aerotherm Div., Acurex Corp., Mountain View, Calif., to be published.

DECEMBER 1974 AIAA JOURNAL VOL. 12, NO. 12

Mathematical Modeling for the Detection of Fish by an Airborne Laser

DAVID L. MURPHREE,* CLAYBORNE D. TAYLOR,† AND RONALD W. MCCLENDON‡

Mississippi State University, Mississippi State, Miss.

To assess the feasibility of an airborne remote sensing laser system for fish detection, a mathematical model was developed and solved which incorporated the physical interactions involved in the process of laser transmission through the air/sea interface and ocean environment. For a circular laser beam incident normal to the ocean surface, the power density was determined beneath the ocean surface as a function of surface roughness (wind velocity) and depth. Using the principle of electromagnetic reciprocity, the power reflected from submerged targets and detected at the airborne receiver was determined. The results from the developed mathematical model, using input parameters of presently available equipment and estimates of fish school density and reflectivity, reveal that the power received at an airborne detector from fish reflected incident laser radiation and the signal-to-noise ratio (S/N) are of sufficient magnitude to locate fish schools with an airborne remote sensing laser system.

I. Introduction

THE recent advances in high-powered lasers operating in the blue-green part of the optical spectrum have led to the possibility of the development of an airborne remote sensing laser system for detection and quantification of objects submerged beneath the ocean surface. The incident laser radiation would be reflected from the submerged objects and detected at an airborne receiver. Such a system would enable location, identification, quantification, and assessment of fish resources.

An aircraft cruising at 160 km/hr while illuminating a 75-m width transverse to the flight direction would search 12 sq km of ocean surface per hour. A 500 pulse/sec laser, illuminating a circular area on the ocean surface of 1 m in diameter per pulse, would thoroughly cover the 75-m width by employing 31 pulses while sweeping the laser beam transverse to the plane's flight direction. The maximum beam angle with respect to the vertical would be 13.8° for a 500-ft altitude. It is necessary to maintain the laser beam diameter on the ocean surface no larger than approximately 1 m in order to maintain a high-power density. The distance between the center of each surface circular illuminated area would be 2.5 m in the transverse direction and 2.7 m in the direction of flight. Underwater beam spreading due to refraction by the distribution of surface facets would insure complete coverage of the underwater regions under investigation.

Received December 26, 1973; revision received June 24, 1974. This research was supported by the National Marine Fisheries Service, Bay St. Louis Fisheries Engineering Laboratory under Contract 03-3-042-27.

Index categories: Lasers; Oceanography, Physical and Biological; Atmospheric, Space, and Oceanographic Sciences.

* Professor of Aerospace Engineering.

† Professor of Electrical Engineering.

‡ Graduate Student, Department of Aerophysics and Aerospace Engineering.

II. Analysis

In order to determine the power density distribution beneath the ocean surface when it is illuminated by a collimated beam of monochromatic light, certain convenient considerations are made. In general, the development followed for the underwater power density is that presented by Swennen.[1]

The ocean surface is considered to be described in terms of a probability distribution of local slopes. Using a Gaussian distribution modified by a Gram-Charlier series to include the effects of wind direction and velocity, Cox and Munk[2] obtained the following empirical relationship for the statistical distribution of slopes on the ocean surface:

$$p(\alpha,\beta)=\frac{e^{-(\xi^2+\eta^2)/2}}{2\pi\sigma_c\sigma_u}\left[1-\tfrac{1}{2}C_{21}(\xi^2-1)\eta-\tfrac{1}{6}C_{03}(\eta^3-3\eta)+\tfrac{1}{24}C_{40}(\xi^4-6\xi^2+3)+\tfrac{1}{4}C_{22}(\xi^2-1)(\eta^2-1)+\tfrac{1}{24}C_{04}(\eta^4-6\eta^2+3)\right] \quad (1)$$

where

$$\xi=\frac{\tan\beta\sin(\alpha-\Psi)}{\sigma_c} \quad (2a)$$

$$\eta=\frac{\tan\beta\cos(\alpha-\Psi)}{\sigma_u} \quad (2b)$$

$$\sigma_c^2=0.003+0.00192W \quad (2c)$$

$$\sigma_u^2=0.00316W \quad (2d)$$